# SUPPLEMENTAL MATERIAL

## Atom-Specific Probing of Electron Dynamics in an Atomic Adsorbate by Time-Resolved X-ray Spectroscopy

Simon Schreck[1], Elias Diesen[2]*, Martina Dell'Angela[3], Chang Liu[1], Matthew Weston[1], Flavio Capotondi[4], Hirohito Ogasawara[5], Jerry LaRue[6], Roberto Costantini[3,7], Martin Beye[8], Piter S. Miedema[8], Joakim Halldin Stenlid[1,2], Jörgen Gladh[1,5], Boyang Liu[1], Hsin-Yi Wang[1], Fivos Perakis[1], Filippo Cavalca[1], Sergey Koroidov[1], Peter Amann[1], Emanuele Pedersoli[4], Denys Naumenko[4], Ivaylo Nikolov[4], Lorenzo Raimondi[4], Frank Abild-Pedersen[2], Tony F. Heinz[5,9], Johannes Voss[2], Alan C. Luntz[2], and Anders Nilsson[1]

[1]Department of Physics, AlbaNova University Center, Stockholm University, SE-10691 Stockholm, Sweden

[2]SUNCAT Center for Interface Science and Catalysis, SLAC National Accelerator Laboratory, 2575 Sand Hill Road, Menlo Park, California 94025

[3]CNR-IOM, SS 14 – km 163.5, 34149 Basovizza, Trieste, Italy

[4]FERMI, Elettra-Sincrotrone Trieste, SS 14 – km 163.5, 34149 Basovizza, Trieste, Italy

[5]SLAC National Accelerator Laboratory, 2575 Sand Hill Road, Menlo Park, California 94025

[6]Schmid College of Science and Technology, Chapman University, Orange, California 92866

[7]Physics Department, University of Trieste, Via Valerio 2, 34127 Trieste, Italy

[8]Deutsches Elektronen-Synchrotron DESY, Notkestrasse 85, Hamburg 22607, Germany

[9]Department of Applied Physics, Stanford University, Stanford, California 94305

*Present address: Fritz-Haber-Institut der Max-Planck-Gesellschaft, Faradayweg 4-6, D-14195 Berlin, Germany. E-mail: diesen@fhi.mpg.de

# CONTENTS

# I. OPTICAL ABSORPTION IN C/Ni

The frequency-dependent dielectric matrix of p4g-C/Ni(100) and clean Ni(100) (with p4g surface layer rotations) were calculated in an independent particle picture from the DFT ground state electronic structures [1]. Using these dielectric tensors, the optical absorption (1-R) for each surface was calculated using Fresnel's equations for the conditions of the experiments (3 degrees angle of incidence with P polarized light). As can be seen in the Figure S1, the optical absorption in C/Ni is nearly indistinguishable from that of Ni and emphasizes that nearly all of the optical absorption for C/Ni occurs in the Ni rather than direct optical excitation of the Ni 3d – C 2p bands.
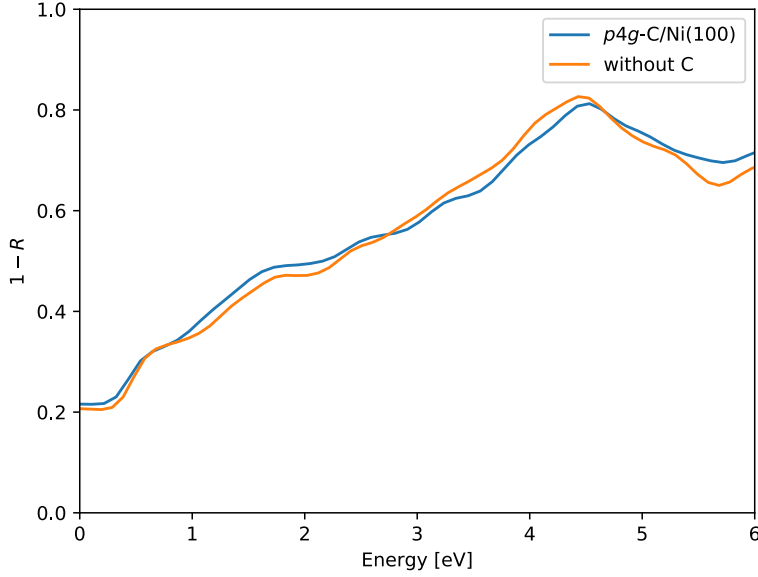
**Fig. S1:** Optical absorption in C/Ni(100) compared to a clean Ni(100) surface.

# II. TWO-TEMPERATURE MODEL

The common two-temperature (2T) model [2] describes the electrons and phonons as two coupled heat baths with depth- and time-dependent temperatures $T_e, T_{ph}$ whose time evolution is governed by the equations:

$$C_e \frac{\partial T_e}{\partial t} = \frac{\partial}{\partial z}\left(\kappa \frac{\partial T_e}{\partial z}\right) - g(T_e - T_{ph}) + S(z,t)$$

$$C_{ph} \frac{\partial T_{ph}}{\partial t} = g(T_e - T_{ph})$$

$$S(z,t) = I(t)e^{-z/\lambda}/\lambda$$

The heat capacity of the phonons is calculated using the Debye model:

$C_{ph} = 9nk_B \left(\frac{T_{ph}}{\Theta_D}\right)^3 \int_0^{\Theta_D/T_{ph}} \frac{x^4 e^x}{(e^x-1)^2}$, where $\Theta_D$ is the Debye temperature of the metal and $n$ the atomic density. The thermal conductivity is written as $\kappa = \kappa_0 \frac{T_e}{T_{ph}}$, with $\kappa_0$ taken as the low temperature value.

The laser pulse is modeled with a Gaussian time profile $I(t) = F\exp(-\frac{t}{2\sigma^2})/\sqrt{2\pi\sigma^2}$, where $F$ is the absorbed fluence on the sample and $\sigma = \Gamma/2.355$ with $\Gamma$ the full width at half maximum (FWHM). The initial temperature was set to 70 K. All other constant parameters are tabulated below. The 2T model is for a pure Ni surface and does not include the modest changes due to the adsorbed C.

The 2T model usually considers a temperature-independent electron-phonon coupling factor $g$, and a simple linear T-dependence of the electron heat capacity $C_e = \gamma T_e$. For Ni a marked departure from this simple behavior has been both observed [3] and found in theoretical studies [4]. We therefore allow a temperature dependent $g(T)$ and $C_e(T)$, using DFT calculations to obtain numerical values for these two quantities (see below).

The resulting temperatures in the surface layer are shown in Fig. S2. We have used the traditional 2T model which only considers the phonon modes of the metal. Adding the phonon modes of the adsorbate C can shorten the time for the $T_{ph}$ rise [5]. However, their inclusion does not affect the rise or peak in $T_e$.
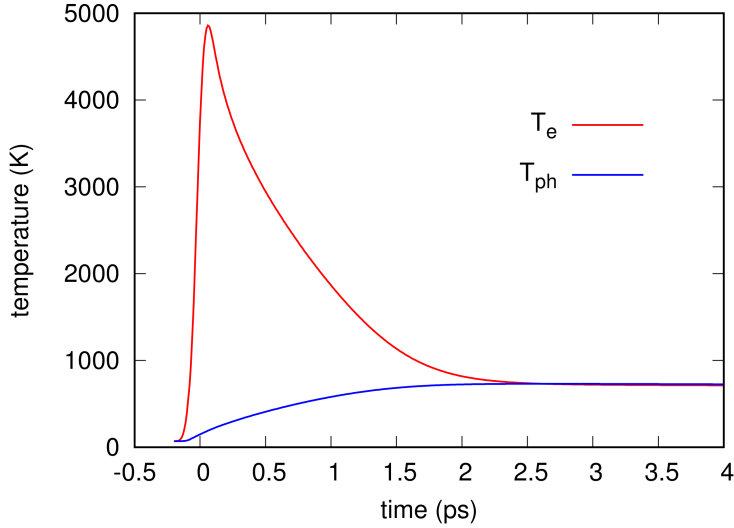


**Fig. S2:** Results from the 2T model with T-dependent parameters.

| $n$ | $9.13 \cdot 10^{28}$ m$^{-3}$ | Atomic density |
|---|---|---|
| $\Theta_D$ | 477.4 K | Debye temperature of Ni |
| $\kappa_0$ | 94 Wm$^{-1}$K$^{-1}$ | Electron heat conductivity |
| $F$ | 126 Jm$^{-2}$ | Absorbed fluence |
| $\lambda$ | 13.49 nm | Optical penetration depth |
| $\Gamma$ | 100 fs | Pulse duration |

**Table SI:** Parameters used in the 2T model

**Properties of Ni**

To accurately model the thermal response of the bulk Ni we use a temperature-dependent electronic specific heat $C_e(T)$ and electron-phonon coupling $g(T)$. In particular for $g$, there are significantly different values in the literature [6–8] due to the separate temperature ranges where different measurement techniques can be applied. To obtain $g(T)$ and $C_e(T)$ as functions of temperature, we calculate the bulk Ni DOS and then follow the approach of Ref. 4. For a given DOS $\rho(E)$, the temperature-dependent Fermi level $\mu(T)$ is given by solving the implicit equation

$$N_e = \int f(E, \mu(T), T)\rho(E)dE$$

where $f$ is the Fermi-Dirac distribution and $N_e$ the number of electrons. We then calculate the heat capacity and electron-phonon coupling as

$$C_e(T) = \frac{\partial U_e}{\partial T} = \frac{\partial}{\partial T}\int f(E, \mu(T), T)\rho(E)EdE$$

$$g(T) = \frac{\pi\hbar k_B\lambda\langle\omega^2\rangle}{\rho(E_F)}\int \rho^2(E)\left(-\frac{\partial f}{\partial E}\right)dE \qquad (S1)$$

where $U_e$ is the internal energy of the electronic system. The quantity $\lambda\langle\omega^2\rangle$ is obtained by matching $g(T)$ at room temperature to experimental data [7].

These quantities were calculated in Ref. 4 using spin-paired calculations for Ni. While this is a crude, but reasonable approximation at temperatures far above the Curie temperature $T \gg T_c$, where the DOS of the paramagnetic state should resemble that of spin-paired Ni and the obtained $C_e(T)$ agrees quite well with experiment (Fig. S3c, experimental results from Ref. 3), for room temperature quantities the DOS from spin-polarized calculations is more accurate so as to avoid the unphysical sharp peak at $E_F$ in the spin-paired DOS (cf. Fig. S3a). Around $T_c$ there should be a smooth transition between the spin-polarized and spin-paired situations. Spin-polarized DFT without treatment of the randomly oriented paramagnetic moments cannot properly account for the paramagnetic phase nor the magnetic phase transition at the experimental Curie temperature $T_c = 631$ K, but rather finds a ferromagnetic ground state up to $T \approx 3000$ K. A complete theoretical treatment of this temperature region requires a treatment of the disordered magnetic moments which is beyond the scope of this work [9]. Note that ultrafast demagnetization [6,10] happens within 20 fs of the driving pulse [11]. Here we take the pragmatic approach of simply dividing the temperature range at the experimental $T_c$. Below this, we use the spin-polarized DOS (summed over the two spins) to calculate $g(T)$ and $C_e(T)$; above it we use the spin-paired DOS. This gives unphysical discontinuities at $T_c$. Since we are however only using our results for the relatively crude 2T model, we find this inaccuracy to be less severe than resorting to a completely spin-paired treatment as in Ref. 4, or using DFT for the full temperature range as in [12], where ferromagnetism persists up to 3000 K giving significant deviations in $C_e(T)$ when compared to experiment. For $C_e(T)$ inclusion of spin has little effect on the results; since we reach temperatures
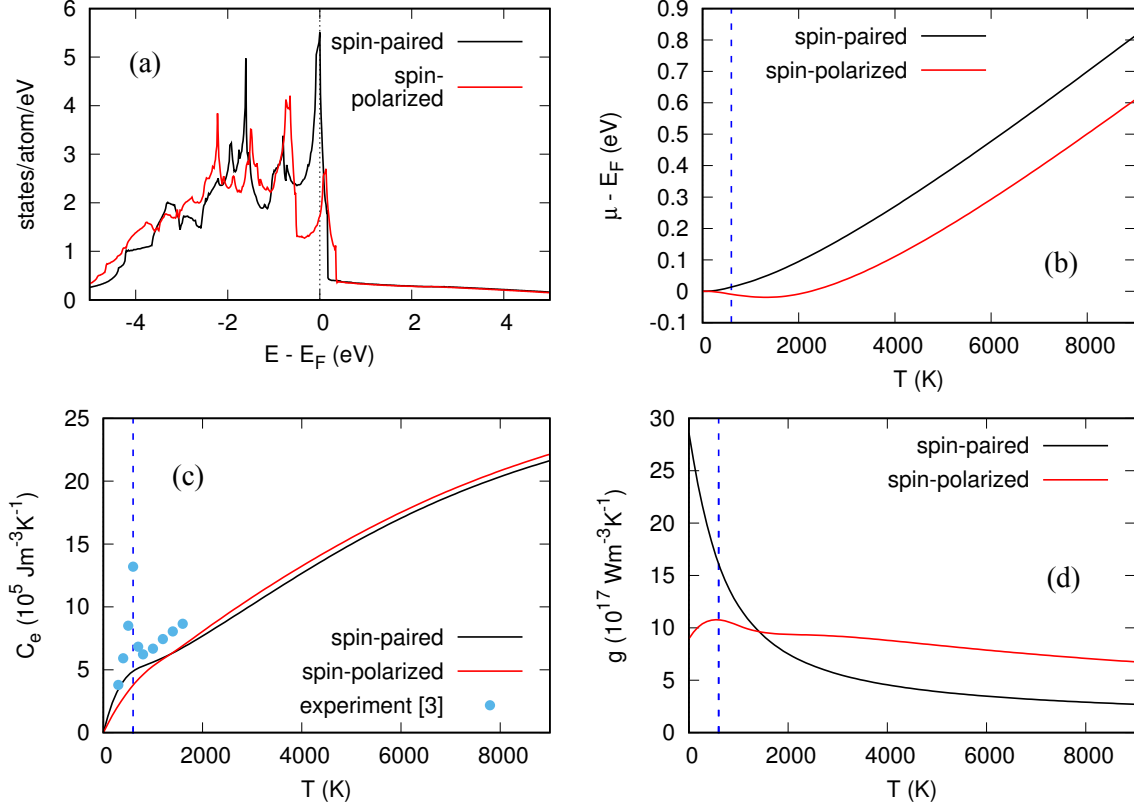
**Fig. S3:** Modelling of high temperature Ni behavior, comparing spin-polarized to unpolarized results. (a) Densities of states (summed over the two spins); (b-d) temperature dependence of the Fermi level, the electronic specific heat, and the electron-phonon coupling g, respectively. The dashed lines indicate the experimental Curie temperature $T_c$; the experimental $C_e(T)$ values are taken from Ref. 3.

$T \approx 5000$ K, some deviations from the correct value for $T < T_c$ will be of little consequence. For $g(T)$ it is more sensitive since the experimental room temperature value of $g$ is used to extract the unknown quantity $\lambda\langle\omega^2\rangle$ in Eq. S1. For this purpose we use the spin-polarized DOS, giving us a value of $\lambda\langle\omega^2\rangle = 91.7$ meV$^2$, compared to $\lambda\langle\omega^2\rangle = 49.5$ meV$^2$ in Ref. 4 where the spin-paired DOS was used also at room temperature. This leads to a stronger electron-phonon coupling, which still compares well with available experiments [6,7]. (Note that, in Ref. 8, a linear $C_e(T)$ was assumed, leading to a significantly underestimated $T_e$ and similarly underestimated $g$.) It is however clear that these parameters are obtained through crude approximations, and the 2T results should therefore only be taken as a rough estimate of the actual temperature evolution of the substrate.

## III. EXPERIMENTAL METHODS

### Experimental Conditions

The optical laser pump and soft X-ray laser probe measurements were performed at the DiProI beamline of the FERMI free-electron laser (FEL) in Trieste, Italy [13]. We used 400 nm optical laser pulses with a pulse duration of 90-100 fs that were generated from the same laser system that is used to seed the FERMI FEL, and soft X-ray pulses in the carbon K-edge photon energy range around 290 eV (4 nm wavelength) with a pulse duration of 45-50 fs. Since seed and pump pulses were generated from the same laser system, the arrival times of the optical laser pump and the FEL X-ray pulse at the sample are intrinsically synchronized. The combined time profile results in an overall resolution of 100-110 fs determined solely by the pulse durations of optical laser and FEL. For X-ray absorption measurements we set the central average FEL photon energy to a number of pre-defined values covering the desired range of the carbon K-edge X-ray absorption resonance with a step size of 0.3 – 0.5 eV. For each photon energy the delay between optical laser and FEL pulse was set to pre-defined values recording 1000 FEL shots for each delay. For X-ray emission measurements we set the central average FEL photon energy to the desired value and varied the delay between optical laser and FEL pulse between pre-defined values recording 1000 FEL shots for each setting. Each delay setting was revisited 10-20 times.

The pump laser had a spot size of $\sim 150 \times 150$ $\mu m^2$ and a pulse energy of $\sim 152$ $\mu J$, and the X-ray probe beam had a spot size of $\sim 30 \times 30$ $\mu m^2$. Both the laser and the x-ray beam had a grazing incidence angle, which was estimated to be 2.24°.

The XAS spectra were recorded by stepwise varying the incidence energy and detecting fluorescence using a large area detector with a perylene filter to remove background UV light. The XES spectra were recorded with a soft X-ray spectrometer similar to the spectrometer previously used at LCLS [14] with an overall resolution of 0.3 eV.

### Sample Preparation

We used established surface science techniques to cover a clean Ni(100) surface with 0.5 ML of carbon that form a p4g(2x2) surface structure. The sample was a standard commercially available Ni(100) single-crystal (from Surface Preparation) with a round surface of 20 mm diameter. The sample was cleaned and prepared in ultra-high vacuum (UHV) condition at a base pressure of $<5 \times 10^{-10}$ mbar. Prior to the experiments initial cleaning of the sample was performed by several tens of cycles of 10 minutes Neon$^+$ sputtering at room temperature followed by 30 minutes of annealing at 600 K. During the experiment the cleaning cycles consisted of Neon$^+$ sputtering at 470 K for 10 minutes followed by flash annealing the sample to 1100 K. After the cleaning procedures, the carbon coverage was prepared by dosing 40 L of $C_2H_2$ at 470 K and thereafter flashing the sample to 650 K to dissociate the $C_2H_2$ into free carbon atoms on the surface. With this procedure a half monolayer

coverage of C on the surface was achieved. After sample preparation the sample was cooled down to liquid nitrogen temperature by a constant liquid nitrogen flow through the cryostat and the experimental chamber was pumped down to its base pressure <5e-10 mbar. No background pressure was applied. Even though the optical laser excitation does not result in irreversible changes of the surface structure we continuously scanned the sample through the laser and FEL beam providing a fresh spot on the sample for each laser and FEL shot-pair. This was done as a precaution to avoid long term heating and possible melting of the substrate. Each spot on the sample was revisited after a cycle period of 10-20 seconds.

**Analysis**

In the post-processing of all recorded data we analyzed the FERMI online spectrometer on a shot-to-shot basis. This spectrometer provides the spectral intensity distribution for each FEL shot, which allowed us to assign an actual central photon energy, bandwidth and intensity for each shot. The analysis showed that, for a fixed average central photon energy, the shot-to-shot fluctuations of the actual central photon energy was ~0.7 eV FWHM and the single-shot FEL bandwidth varied between 0.2 and 1.0 eV FWHM. We used the single-shot values to filter out shots with low intensity or large FEL bandwidth (FWHM>0.6 eV). For X-ray emission measurements we filtered out in addition shots for which the actual central photon energy was off from the desired photon energy by more than ±0.15 eV. For X-ray absorption measurements we resorted all shots based on their actual central photon energy into bins of 0.25 eV width. For each bin the accumulated Total Fluorescence Yield (TFY) intensity was normalized by the accumulated incident intensity and the standard error was calculated based on Poisson statistics.

The transient changes in XAS and XES intensity in Figure 3 were modeled with a sum of two Gaussian error functions of the form $I(t) = a \cdot \int_{-\infty}^{t} e^{-(t-t_0)/\sigma^2}$. We used Gaussian fitting for the rise and decay in order to mimic the resolution of the convoluted two laser pulses and to observe if there are any additional delays beyond the instrumental time broadening. Only the blue delay trace in Figure 3(a) was modeled by a single Gaussian error function. We denote the value for $\sigma$ as the characteristic rise or decay time and $t_0$ as the edge position representing the inflection point of the rising or falling flank.

# IV. COMPUTATIONAL METHODS

**Spectrum calculations at equilibrium positions**

To identify the dynamics causing changes in the XAS and XES, we calculate X-ray spectra using GGA-level density functional theory (DFT) calculations and the transition-potential (TP) approach [15]. This method has been successfully used to identify detailed structural changes in adsorption via X-ray spectroscopy [16] and for interpretation of the ultrafast evolution of X-ray spectra in terms of underlying dynamical features [17–20].

We mainly use the DFT code Quantum ESPRESSO [21,22], which uses a plane-wave basis for the valence electrons and pseudopotentials to represent the core electrons. We use the RPBE [23] functional due to its accuracy in determining surface adsorption energies [24]. All calculations are spin-polarized (unrestricted Kohn-Sham). We use a four-layer 2x2 slab model for initial geometry optimization, with C/Ni adsorbed in four-fold hollow sites at ½ ML coverage, with periodic boundary conditions in all directions and 20 Å of vacuum separating the slab from its periodic image. An RPBE optimimum lattice constant of 3.553 Å for bulk fcc-Ni was used, and a 4x4x1 Monkhorst-Pack grid for Brillouin zone integration. Optimizing the atomic positions correctly predicts the p4g surface restructuring upon adsorption of C on the Ni(100) surface. For the excited-state calculations, we double the cell in the x- and y-directions to 4x4x4 (correspondingly reducing the k-point grid to 2x2x1) to reduce the interaction of the core hole with its periodic images. XAS spectra were computed using a refined 11x11x1 k-point grid, while keeping the density fixed (non-SCF/Harris calculation). Ultrasoft pseudopotentials [25] were used for atoms without core excitations. The plane-wave and density cutoffs were correspondingly chosen for the surface calculations to be 500 and 5000 eV, respectively. The geometries were optimized until all forces were less than 0.01 eV/Å, with the bottom two layers kept fixed.

The XAS is calculated using a Lanczos recursion Green's function technique, as implemented in the xspectra code [26–28]. For the spectrum calculations, a half-core-hole pseudopotential was used on the excited atom (transition-potential approach [15]) which has been shown to give reliable results [15,29]. For the core-excited C, norm-conserving half and full core-hole pseudopotentials were generated using the 'atomic' code included with the Quantum Espresso distribution [21]. Full and half-core hole pseudopotentials are generated by occupying the 1s shell in the single-atom DFT solution by only, respectively, 1 and 1.5 electrons. The obtained spectra were shifted according to our calculated absorption onsets (Δ-Kohn-Sham method). All spectra were finally shifted by a common reference energy, chosen in order to match the experimental spectrum at negative delay with the calculated spectrum of the adsorbate in its optimized position.

XES is calculated in an analogous way using xspectra, however no Δ-Kohn-Sham procedure is needed since the core binding energy does not enter into the final XES emission energy [30]. Furthermore, no explicit core hole pseudopotential is needed since the final state of XES decay contains a ground state

core [31]. For this reason the spectrum calculation can be performed using the 2x2x4 slab model. An overall shift is performed also for the XES to align with the experimental unpumped spectra, and an overall broadening is applied to account for lifetime effects and instrumental resolution. C/Ni does not get significantly vibrationally excited during the XES process [32,33], allowing for the simplified treatment used here without the need for the full Kramers-Heisenberg formalism.

For calculating the parameters of the 2T model, calculations for bulk Ni were performed using the VASP code [34,35] with ultrasoft (PAW) pseudopotentials [36]. An elementary fcc unit cell and a 21x21x21 k-point grid was used, with the Blöchl tetrahedron method [37] to obtain the density of states.

**Spectrum calculations at $T_e = 5000$ K**

To simulate the effect of a high electronic temperature on XAS and XES, we first obtain the electronic density from an ordinary DFT calculation with the electronic states populated according to a 5000 K Fermi-Dirac distribution. The presence of holes below and electrons above the Fermi level ($E_F$) affects XAS and XES in opposite ways. In XAS the excited core electron can now populate states below $E_F$ that would already be filled at low temperature, increasing the XAS intensity there; above $E_F$ the fact that some states are already filled instead lowers the XAS intensity. In XES the reverse is seen: the intensity above $E_F$ is increased while the intensity below decreases. These effects are included in the spectrum calculation by explicitly including the thermal occupation numbers when calculating the X-ray transition rates.

**Spectrum calculations at $T = 800$ K**

To simulate the effect of an equilibrated hot system with both electrons and phonons thermalized, corresponding to the situation at $t > 2$ ps, we perform an *ab initio* molecular dynamics (AIMD) simulation using VASP. The cell was identical to the one used in Quantum ESPRESSO for optimization. Starting at the equilibrium geometry with randomized initial velocities corresponding to a Maxwell-Boltzmann distribution at the desired temperature of 800 K, we use a Langevin thermostat to simulate a thermal ensemble. After equilibrating the system for 1 ps, the dynamics was run for another 1 ps with a time step of 2 fs. Every 100 fs, the structure was saved and the XAS and XES were calculated for that static structure using the Quantum ESPRESSO package. These spectra were then averaged together for the final result.

# V. XAS FROM DIFFERENT ADSORBATE GEOMETRIES

To investigate the origin of the additional intensity at energies above the main XAS peak in the experimental 4.0 ps delay spectrum, and the corresponding shift in the spectrum from AIMD, we calculate the XAS at intermediate geometries as the C atom moves from the hollow to a bridge site. At high temperatures, both motion of substrate atoms and of the adsorbate itself will contribute to the C moving out of the hollow site. We calculate the XAS for the p4g geometry and three intermediate geometries (ptb-1, ptb-2 and ptb-3) between p4g and the geometry where one C atom is moved to a nearby bridge site, along the minimum energy path obtained with a nudged elastic band (NEB) simulation. The structures are shown in Figure S4. The displacement of the C atom from the p4g geometry for ptb-1, ptb-2 and ptb-3 are 0.32 Å, 0.90 Å and 1.56 Å, respectively. These calculations were performed using the GPAW [38,39] code; the computational parameters were the same as for other calculations (see Supplement IV). Franck-Condon transitions into vibrationally excited states perpendicular to the surface were taken into account in the following way: For each geometry, the carbon atom is vertically displaced from -0.5 Å to +1.5 Å from the original position, and the potential energy and the XAS are calculated for every displacement point (41 in total). The vibrational eigenstates on the ground and excited PES are then calculated numerically, and the eigenfunction overlap gives the Franck-Condon factors. The vibrational excitations turn out to have limited influence on the spectra, consistent with experimental results [32]. Finally, a Gaussian broadening of 1.05 eV and a Lorentzian broadening of 0.3 eV were applied to the obtained spectra.

All computed theoretical XAS curves are plotted together with the experimental XAS at the negative time delay –0.4 ps in Figure S5. The p4g geometry gives a main peak at around 283.6 eV. When the C atoms moves towards the nearby bridge site, the peak position moves towards higher energies, which corresponds to the increase in intensity in the experimental result at around 284.6 eV.
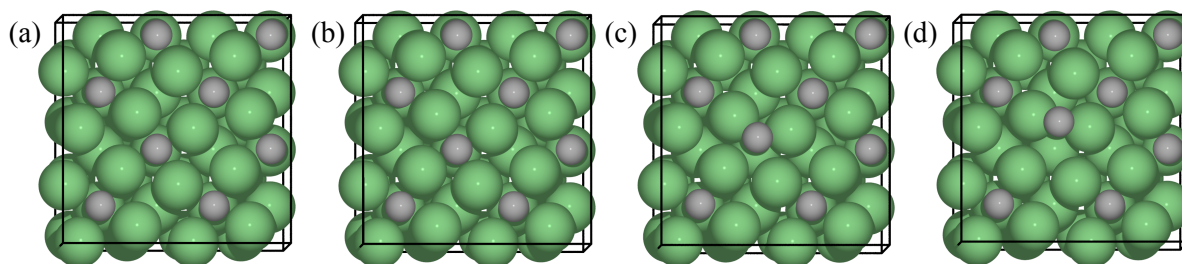


**Figure S4:** Atomic models for (a) p4g C/Ni, the intermediate geometries from p4g to bridge (b) ptb-1, (c) ptb-2, and (d) ptb-3. The green and black spheres represent Ni and C atoms, respectively. The ptb-3 geometry is very close to the bridge geometry but not exactly at the bridge site.
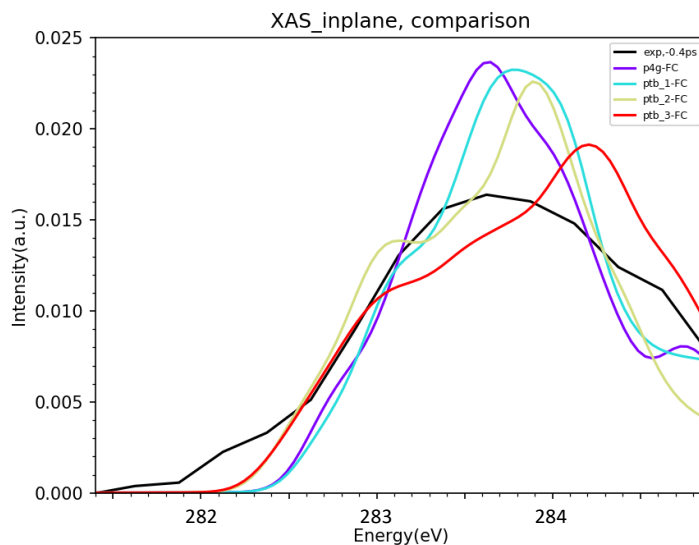
**Figure S5:** Experimental XAS at the delay –0.4 ps, and the computed XAS for the geometries shown in Figure S4.

# VI. SELECTIVE VIBRATIONAL EXCITATION OF ADSORBATES

We propose ultrafast excitation of in-plane C vibrations as a possible explanation for the very rapid redshift observed in the XES. In this section we describe the details of the spectra obtained by selectively exciting particular vibrational modes of the C atoms, and models for energy transfer from the excited electrons of the substrate to these vibrational modes (=phonons). Neither our electronic friction model with calculated electron-phonon couplings nor an ion-resonance model where excited electrons directly populate the antibonding C-Ni resonance can quantitatively reproduce this very fast (< 0.25 ps) and selective excitation of the C in-plane vibration. However, ultrafast vibrational excitation (~100 fs) of adsorbate modes has been observed previously [20,40,41], suggesting that ballistic non-thermalized electrons formed initially by the optical laser excitation of the metal could couple much more strongly to adsorbate motion than the thermalized hot electrons described by an electronic frictional coupling.

**Spectra from vibrationally excited adsorbates**

To calculate the spectrum resulting from a vibrationally excited adsorbate, we follow a similar method as in Ref. 20. We first observe that, in the optimized structure, the C atoms occupy the four-fold hollow sites almost in plane with the top layer Ni atoms. A vibrational analysis allowing only one C atom to vibrate gives two degenerate eigenfrequencies 20.48 THz for in-plane ($x,y$) vibrations, and 9.35 THz for out-of-plane ($z$) vibrations. For obtaining approximate spectra we assume that each C vibrates independently of each other in a cylindrically symmetric potential. Due to the anharmonicity
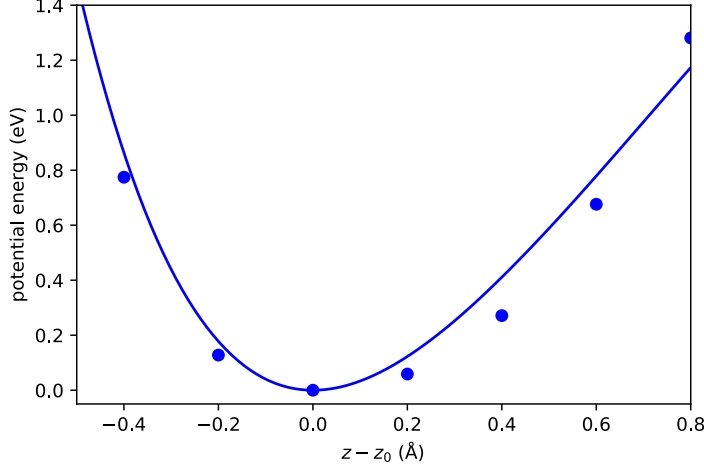
**Fig. S6:** The calculated PES (dots) and Morse potential fit (solid) in the out-of-plane direction

of the potential in $z$-direction, the potential energy was calculated for several displacements, and a Morse potential $V(z) = D_e(1 - e^{-a(z-z_0)})$ was fitted to the values. The obtained potential is shown in Fig. S6. The vibrational states are then analytically given by:

$$\psi_n^{(gs)}(z) = N_n z^{\lambda-n-\frac{1}{2}} e^{-\frac{z}{2}} L_n^{(2\lambda-2n-1)}(z)$$

where $z = 2\lambda e^{-(x-x_0)}$; $x = ar$; $\lambda = \frac{\sqrt{2mD_e}}{a\hbar}$ ($m$ is the mass of C); $N_n = \sqrt{\frac{n!(2\lambda-2n-1)}{\Gamma(2\lambda-n)}}$ and $L_n^\alpha(z)$ is a generalized Laguerre polynomial.

The in-plane vibration was modeled using a radially symmetric quadratic potential corresponding to frequency 20.48 THz in the radial direction, giving a 2D harmonic oscillator. Its eigenstates can be written in terms of the radial coordinates $(r, \varphi)$ as [42]:

$$\chi_{n,M}(r, \varphi) = C_{p,M} \theta^{|M|} e^{-\frac{\lambda r^2}{2}} L_p^{|M|}(\lambda r^2) e^{iM\varphi}$$

where $\lambda = m\omega/\hbar$, $p = (n - |M|)/2$, $C_{p,M} = \sqrt{\frac{2\lambda^{|M|+1}p!}{(p+|M|)!}}$ and $L_p^{|M|}$ is the generalized Laguerre function.

$M$ takes the values $-n, -n+2, ..., n-2, n$ giving an $n + 1$-fold degeneracy of the $n^{th}$ level. The energy levels are given by $E_n = \hbar\omega(n + 1)$, with $n = 0,1,2, ...$.

For the perpendicular direction we then calculate the spectra $w(E, z)$ for a number of displacements. We interpolate the result to get a continuous 2D function, and then calculate the spectrum $w_n(E)$ for each vibrational state as:

$$w_n(E) = \int w(E, z) |\psi_n^{(gs)}(z)|^2 dz \qquad (S2)$$

For the in-plane direction we calculate in an analogous way the spectra for radial displacements $w(E, x)$. We approximate the dependence on the azimuthal angle $\varphi$ as $w(E, r, \varphi) \approx w(E, x)\cos^2\varphi + w(E, y)\sin^2\varphi$. For a single state $\chi_{n,M}$ we then get

$$w_{n,M}(E) = \int w(E, r, \varphi) |\chi_{n,M}(r, \varphi)|^2 r d\varphi dr \propto \int (w(E, x) + w(E, y)) |\chi_{n,M}(r)|^2 r dr$$

since $|\chi_{n,M}|^2$ is independent of $\varphi$. Writing $w(E,r) \equiv w(E,x) + w(E,y)$ we then calculate the total spectrum in a similar way to Eq. S2. We need to sum over all allowed $M$-values for each $n$, which yields the following expression

$$w_n(E) = \sum_M \int w(E,r)|\chi_{n,M}(r)|^2 r\,dr$$

To finally calculate the spectrum at an elevated temperature T, the spectra from the individual states are added together according to the Boltzmann distribution to give:

$$w(E,T) = \sum_n P_n(T)w_n(E) \quad \text{with } P_n(T) = \frac{e^{-E_n/k_B T}}{\sum_n e^{-E_n/k_B T}}$$

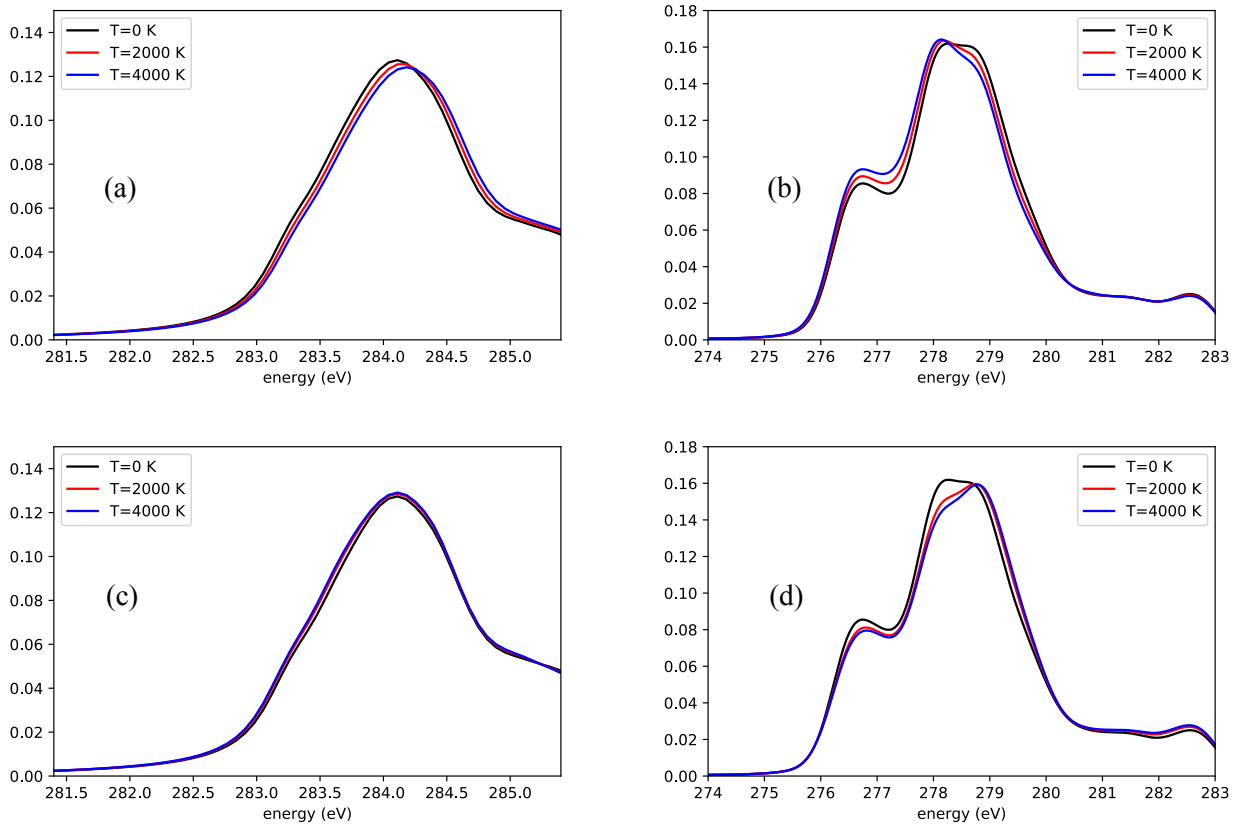The resulting spectra are shown in Fig. S7 for T=0 K, 2000 K and 4000 K.



**Fig. S7:** Calculated XAS (left) and XES (right) with vibrationally high temperature. (a) and (b): excited in-plane vibration; (c) and (d); excited out-of-plane vibration.

**Calculation of lifetimes of adsorbate modes by electron-phonon coupling**

We calculate the theoretical lifetimes of the C/Ni(100) adsorbate vibrational modes using the DFPT [43] method implemented in Quantum ESPRESSO. Details on the method and its implementation can be found in e.g. [44,45]. Our approach has been described in detail in Ref. 20. The phonon linewidth $\gamma_{q\nu}$ is calculated by evaluating the Fermi-golden-rule-like expression

$$\gamma_{qv} = 2\pi\omega_{qv} \sum_{ij} \int \frac{d^3\boldsymbol{k}}{\Omega_{BZ}} \left| g_{qv}(\boldsymbol{k}, i, j) \right|^2 \delta(E_{\boldsymbol{q},i} - E_F)\delta(E_{\boldsymbol{k}+\boldsymbol{q},j} - E_F) \tag{3}$$

where $g_{qv}(\boldsymbol{k}, i, j)$ are the electron-phonon coefficients. The double-delta expression in Eq. 3 is evaluated by replacing the delta functions by Gaussian functions of width σ (for our results, σ=0.6 eV was used). We use a 16x16x1 k-point grid to evaluate the linewidths, using the interpolation scheme described in Ref. 45. Since the electron-hole pair scattering can excite phonons at any $\boldsymbol{q}$, we calculate $\gamma_{qv}$ for a grid of points in the first Brillouin zone and average the result:

$$\bar{\gamma}_v = \int \frac{d^2\boldsymbol{q}}{\Omega_{BZ}}\gamma_{qv}$$

from which we get the lifetime as $\tau_v = \hbar/\bar{\gamma}_v$.

The obtained lifetimes of the highest frequency modes are shown in Table SII. The first four modes correspond to in-plane vibrations of the two carbon atoms, while the following two modes are symmetric and asymmetric out-of-plane vibrations. Due to the relatively small mass difference between C and Ni, especially the out-of-plane vibrations are somewhat mixed with substrate vibrations. However the obtained values give at least a semi-quantitative estimate of the relative coupling strengths. The modes with lower frequencies, dominated by substrate vibrations, have lifetimes in the range 4.5-6 ps.

| Lifetime (ps) | Mode character |
|---|---|
| 1.74 | In-plane |
| 1.71 | In-plane |
| 2.65 | In-plane |
| 3.93 | In-plane |
| 3.05 | Out-of-plane |
| 2.39 | Out-of-plane |

**Table SII:** Calculated lifetimes of the six highest frequency modes.

**Ion resonance model for adsorbate excitation**

A common picture for the coupling between excited electrons and adsorbate motion is the ion resonance model, where a single energetic electron resonantly populates an unoccupied orbital of the adsorbate. This is the mechanism behind the Desorption Induced by (Multiple) Electronic Transitions (DIET [46,47] and DIMET [48]) processes. Within this picture, we can get an estimate of the energy transfer to the adsorbate IS mode due to resonant population of the adsorbate LUMO by scattering of excited electrons from the substrate into the resonance. To this end, we calculate the potential energy surface (PES) for the C using the linear-expansion ΔSCF method [49], which ensures that an empty C p-derived orbital is populated by one electron. The GPAW code [38,39] was used for the excited-state PES calculation, using identical parameters to the Quantum ESPRESSO calculations in the rest of this

work. To define the orbital to be filled, an SCF calculation is first done removing all atoms except one C from the unit cell. This will give 3 p-bands (one with $p_z$ character and two with $p_{xy}$ character) with weak dispersion since the C interact with its periodic image; we consider the resulting densities at the gamma point as a sufficiently good approximation of the atomic orbital, which is then having a constrained occupation = 1 in the following ΔSCF calculation. The resulting PES curves with each of the three bands populated are shown in Fig. S8. The equilibrium in-plane position of the adsorbate is unchanged since it is dictated by the fourfold symmetry of the adsorption site; furthermore the interaction strength is also little affected, giving a largely unchanged PES. We thus rule out this mechanism for driving in-plane motion.
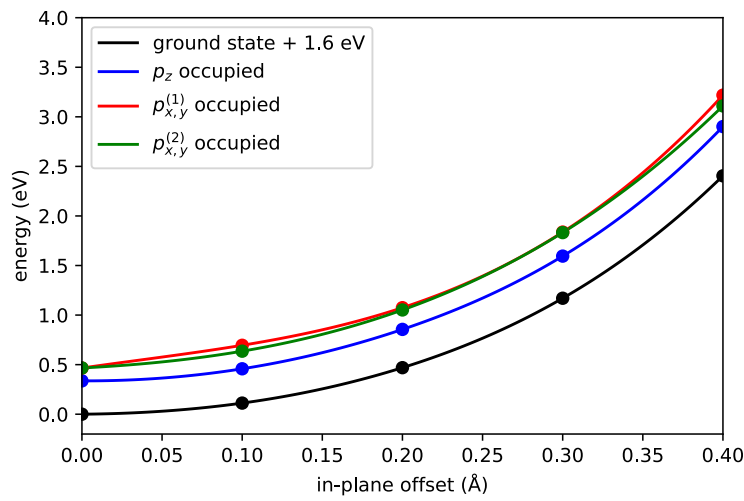


**Fig. S8:** Potential energy curves obtained using the ion resonance model, for the ground state and when populating the three C p-derived orbitals. The ground state curve has been shifted upwards by 1.6 eV to allow easy comparison of the curve shapes.

# REFERENCES

[1]    M. Gajdoš, K. Hummer, G. Kresse, J. Furthmüller, and F. Bechstedt, Phys. Rev. B - Condens. Matter Mater. Phys. **73**, 045112 (2006).

[2]    S. I. Anisimov, B. L. Kapeliovich, and T. L. Perel'man, Zh. Eksp. Teor. Fiz. **66,** 776 (1974) [Sov. Phys.-JETP **39**, 375 (1974)].

[3]    G. K. White, Int. J. Thermophys. **9**, 839 (1988).

[4]    Z. Lin, L. V. Zhigilei, and V. Celli, Phys. Rev. B - Condens. Matter Mater. Phys. **77**, 075133 (2008).

[5]    D. Novko, J. C. Tremblay, M. Alducin, and J. I. Juaristi, Phys. Rev. Lett. **122**, 016806 (2019).

[6]    E. Beaurepaire, J.-C. Merle, A. Daunois, and J.-Y. Bigot, Phys. Rev. Lett. **76**, 4250 (1996).

[7]    A. P. Caffrey, P. E. Hopkins, J. M. Klopf, and P. M. Norris, Nanoscale Microscale Thermophys. Eng. **9**, 365 (2005).

[8]    S.-S. Wellershoff, J. Güdde, J. Hohlfeld, J. G. Müller, and E. Matthias, Proc. SPIE **3343**, 378 (1998).

[9]    I. A. Abrikosov, A. V. Ponomareva, P. Steneteg, S. A. Barannikova, and B. Alling, Curr. Opin. Solid State Mater. Sci. **20**, 85 (2016).

[10]   B. Koopmans, G. Malinowski, F. Dalla Longa, D. Steiauf, M. Fähnle, T. Roth, M. Cinchetti, and M. Aeschlimann, Nat. Mater. **9**, 259 (2010).

[11]   W. You et al., Phys. Rev. Lett. **121**, 077204 (2018).

[12]   P. Scheid, G. Malinowski, S. Mangin, and S. Lebègue, Phys. Rev. B **99**, 174415 (2019).

[13]   E. Allaria et al., Nat. Photonics **6**, 699 (2012).

[14]   T. Katayama et al., J. El. Spect. Rel. Phen. **187**, 9 (2013).

[15]   L. Triguero, L. G. M. Pettersson, and H. Ågren, Phys. Rev. B **58**, 8097 (1998).

[16]   E. Diesen, G. L. S. Rodrigues, A. C. Luntz, F. Abild-Pedersen, L. G. M. Pettersson, and J. Voss, AIP Adv. **10**, 115014 (2020).

[17]   H. Öström et al., Science **347**, 978 (2015).

[18]   A. Nilsson et al., Chem. Phys. Lett. **675**, 145 (2017).

[19]   H. Öberg et al., Surf. Sci. **640**, 80 (2015).

[20]   E. Diesen et al., Phys. Rev. Lett. **127**, 016802 (2021).

[21]   P. Giannozzi et al., J. Phys. Condens. Matter **21**, 395502 (2009).

[22]   P. Giannozzi et al., J. Phys. Condens. Matter **29**, 465901 (2017).

[23]   B. Hammer, L. B. Hansen, and J. K. Nørskov, Phys. Rev. B **59**, 7413 (1999).

[24]   S. Mallikarjun Sharada, R. K. B. Karlsson, Y. Maimaiti, J. Voss, and T. Bligaard, Phys. Rev. B **100**, 035439 (2019).

[25]   D. Vanderbilt, Phys. Rev. B **41**, 7892 (1990).

[26]   M. Taillefumier, D. Cabaret, A.-M. Flank, and F. Mauri, Phys. Rev. B **66**, 195107 (2002).

[27]   C. Gougoussis, M. Calandra, A. P. Seitsonen, and F. Mauri, Phys. Rev. B **80**, 075102 (2009).

[28]   O. Buñau and M. Calandra, Phys. Rev. B **87**, 205105 (2013).

[29]   M. Leetmaa, M. P. Ljungberg, A. Lyubartsev, A. Nilsson, and L. G. M. Pettersson, J. El. Spect. Rel. Phen. **177**, 135 (2010).

[30]   L. Triguero, L. G. M. Pettersson, and H. Ågren, J. Phys. Chem. A **102**, 10599 (1998).

[31]   A. Föhlisch, J. Hasselström, P. Bennich, N. Wassdahl, O. Karis, A. Nilsson, L. Triguero, M. Nyberg, and L. Pettersson, Phys. Rev. B - Condens. Matter Mater. Phys. **61**, 16229 (2000).

[32]   A. Nilsson and N. Mårtensson, Phys. Rev. Lett. **63**, 1483 (1989).

[33]   A. Nilsson and L. G. M. Pettersson, Surf. Sci. Rep. **55**, 49 (2004).

[34]   G. Kresse and J. Furthmüller, Phys. Rev. B **54**, 11169 (1996).

[35]  G. Kresse and J. Furthmüller, Comput. Mater. Sci. **6**, 15 (1996).

[36]  G. Kresse and D. Joubert, Phys. Rev. B - Condens. Matter Mater. Phys. **59**, 1758 (1999).

[37]  P. E. Blöchl, O. Jepsen, and O. K. Andersen, Phys. Rev. B **49**, 16223 (1994).

[38]  J. J. Mortensen, L. B. Hansen, and K. W. Jacobsen, Phys. Rev. B **71**, 035109 (2005).

[39]  J. Enkovaara et al., J. Phys. Condens. Matter **22**, 253202 (2010).

[40]  K.-i. Inoue, K. Watanabe, and Y. Matsumoto, J. Chem. Phys. **137**, 024704 (2012).

[41]  K.-i. Inoue, K. Watanabe, T. Sugimoto, Y. Matsumoto, and T. Yasuike, Phys. Rev. Lett. **117**, 186101 (2016).

[42]  See e.g. S. Flügge, *Practical Quantum Mechanics* (Springer-Verlag Berlin Heidelberg, 1971), p. 107-110.

[43]  S. Baroni, S. de Gironcoli, A. Dal Corso, and P. Giannozzi, Rev. Mod. Phys. **73**, 515 (2001).

[44]  M. Calandra and F. Mauri, Phys. Rev. B **71**, 064501 (2005).

[45]  M. Wierzbowska, S. de Gironcoli, and P. Giannozzi, ArXiv Prepr. Cond-Mat/0504077 (2005).

[46]  D. Menzel and R. Gomer, J. Chem. Phys. **41**, 3311 (1964).

[47]  P. A. Redhead, Can. J. Phys. **42**, 886 (1964).

[48]  J. A. Misewich, T. F. Heinz, and D. M. Newns, Phys. Rev. Lett. **68**, 3737 (1992).

[49]  J. Gavnholt, T. Olsen, M. Engelund, and J. Schiøtz, Phys. Rev. B **78**, 075441 (2008).